


Molecular potential anisotropy probed by electron rescattering in strong-field ionization of molecules

C. Cornaggia *Université Paris-Saclay, CEA, CNRS, LIDYL, CEA Paris-Saclay, bâtiment 522, 91191 Gif-sur-Yvette, France* (Received 3 August 2020; revised 24 November 2020; accepted 14 December 2020; published 7 January 2021)

One of the main differences between rescattering following laser-induced ionization of atoms and molecules and electron-ion collisions performed with electron beams is the quivering dynamics of the electron around the ionic site in laser experiments. This report is aimed at probing the effect of the anisotropic potential of linear and symmetric molecular ions on the departing electron following tunnel ionization and rescattering by an intense femtosecond laser field at $0.8\ \mu\text{m}$ and $10^{14}\ \text{Wcm}^{-2}$. The laser excitation conditions are chosen so that the maximum collision energy remains of the order of 20 eV. In the energy range where rescattering is significant, the angular widths of the photoelectron angle-resolved energy spectra are found to be significantly larger for N_2 and C_2H_2 molecules aligned perpendicularly to the laser polarization than the angular widths of angle-resolved energy spectra recorded in parallel alignment, although N_2 and C_2H_2 obey opposite tunnel ionization dynamics with respect to alignment. In the associated collision energy and angle ranges where this effect is observed, the lowest values of the impact parameter are less than one atomic unit. It is conjectured that the approach of the quivering departing electron may be sufficient for its trajectories to be dependent on the molecular ion core alignment, i.e., the anisotropic molecular potential.

DOI: [10.1103/PhysRevA.103.013102](https://doi.org/10.1103/PhysRevA.103.013102)

I. INTRODUCTION

Electron scattering on atoms and molecules at energies ranging from 1 eV to 1 keV is of particular interest in many fields of physics, chemistry, and biochemistry from modeling plasma in thermonuclear reactors to radiation-induced damage in biological materials [1]. Differential cross sections for the different output channels of the electron-molecule interaction are calculated from *ab initio* multielectron quantum models and are continuously compared to the differential cross sections measured with electron beams in order to get a reliable data base [2].

In parallel to this very active research field, electron scattering was found in the 1990s to play a central role in the interaction of atoms and molecules with intense infrared linearly polarized laser pulses [3–5]. New relaxation channels in addition to single ionization and direct electron ejection, such as non-sequential double ionization, high-order harmonic generation, and high-order above-threshold ionization were successfully explained in terms of the laser-driven rescattering dynamics of the ionized electron onto the remaining ion core. For a review see, e.g., Ref. [6]. Once in the continuum, the electron freed from tunnel ionization oscillates in the linearly polarized laser field, acquires kinetic energy, and revisits the ion core. The subsequent scattering if any, usually denoted rescattering, may be inelastic through conversion of kinetic energy in recombination with the ion core leading to VUV-XUV high-order harmonic generation or ejection of a second electron leading to nonsequential double ionization. Rescattering may be elastic and lead to high-order above-threshold ionization as demonstrated in the pioneering work of Paulus *et al.* [7]. This report is devoted to this last rescattering channel.

The rescattering electron wave packet is intrinsically coherent and exhibits a large energy spectrum up to $3.17U_p$, where U_p is the ponderomotive energy scaling as the laser intensity times the square of the wavelength. For a typical intensity of $10^{14}\ \text{Wcm}^{-2}$, the maximum recollision energy ranges from a few tens of electronvolts in the near infrared, 19 eV at $0.8\ \mu\text{m}$ the wavelength used in this work, to a few hundreds of electronvolts in the mid-infrared. The direct electron signal from electron waves which have not been rescattered dominates the energy spectrum and decreases within $2U_p$, which is the classical maximum energy associated to direct ionization. Then the energy spectrum exhibits a descending plateau with a maximum energy around $10U_p$, which corresponds to the classical maximum energy of the backscattered electron signal at 180° . The good agreement of the limit energy values of direct and rescattered electron signals from classical kinematics with the values from experiments and quantum calculations are mainly due to the dominating laser field. This agreement naturally appears in the quantum approach of the so-called strong-field approximation theory (SFA) and the associated saddle-point procedures for the evaluation of the action of the electron in the laser field [8–10].

Soon after the appearance of the rescattering model, Zuo *et al.* proposed to use the elastic rescattering channel as an ultrafast structural probe of the molecular ion and labeled the new method laser-induced electron diffraction (LIED) [11]. In the 2000s, Chen *et al.* established from extensive quantum simulations that it is possible to extract field-free differential cross sections from the high-energy plateaus of electron spectra [12,13]. This new so-called quantitative rescattering theory (QRS) lead to measurements of differential cross sections in atoms and molecules [14–17], and more recently

to laser-induced electron diffraction equivalent to conventional electron diffraction with rescattering energies larger than 100 eV using mid-infrared laser pulses with femto- to attosecond temporal resolution [18–20].

The objective of the present paper is to study the influence of the anisotropy of the molecular ionic potential on the departure of the rescattering electron from the molecular site. Indeed one of the main differences with experiments using electron beams is the quivering dynamics of the laser-driven rescattering electron before and after the rescattering event. In the regime of electron diffraction with relatively high rescattering energies larger than 100 eV and in consequence fast electron departure from the molecular site, the influence of the potential anisotropy is expected to be of minor importance. Of course, the molecular potential encodes the electron diffraction pattern, the aspect of which is not within the scope of this paper. Lower scattering energies may favor Coulomb focusing and in consequence multiple returns, thus enhancing the influence of the anisotropic molecular potential [21–23]. In the recent study of Hao *et al.*, it is shown that the second, third, and fourth returns have higher contributions than the first return to the rescattering signal for pulses as short as 25 fs at 0.8 μm for energies up to $6U_p$ for the second and fourth returns and $10U_p$ for the third return [23]. Therefore we choose to work at this wavelength with a pulse duration of 40 fs. With maximum recolliding energies of the order of 20 eV, the minimum de Broglie wavelength of the electron is of the order of 2.7 Å and rules out the electron diffraction regime for molecules with bond lengths of the order of 1 Å.

The potential anisotropy is expected to be effective at small distances between the scattering electron and the ion while at large distances the Coulomb field of the molecular ion is isotropic. Small-angle forward scattering takes place for large impact parameters, when the electron keeps far away from the target ion. Therefore, we will be interested by large-angle scattering corresponding to small impact parameters where the electron closely approaches the target and thus can feel the anisotropic potential. Since the collision angle is not directly accessible in experiments, the energy and angle ranges of the detected electron signal will be detailed below.

We choose two linear molecules N_2 and C_2H_2 remaining linear once ionized, but with different ionization dynamics in order to look for similarities and differences associated to rescattering in the case of two linear ionic targets. The tunnel ionization dynamics is governed by the highest occupied molecular orbital (HOMO) of the molecule [24–26]. The HOMO of N_2 is a $3\sigma_g$ orbital which is preferentially ionized when the molecular axis is parallel to the laser polarization [25], while the HOMO $1\pi_u$ of C_2H_2 favors the ionization when the molecular axis is perpendicular to the laser field [27]. This strategy is based upon the fact that the recolliding wave packets are thus expected to be different in N_2 and C_2H_2 because the nodal structures of the associated HOMOs are different. Recently Bredtmann and Patchkovskii have shown that the HOMO symmetry imposes a phase structure on the recolliding electron wave packet which modifies rescattering [28]. Therefore the comparison between the rescattered spectra of both molecules is expected to distinguish the common features of the anisotropic Coulomb potential from the molecular-dependent signatures.

TABLE I. Experimental parameters for N_2 and C_2H_2 . Laser intensity: I , maximum classical kinetic energy of direct electron: $2U_p$, ionization potential: I_p , Keldysh adiabaticity parameter: γ , and transverse momentum width from tunnel ionization: σ_\perp in atomic units (a.u.).

Molecule	I (10^{14} Wcm^{-2})	$2U_p$ (eV)	I_p (eV)	γ	σ_\perp (a.u.)
N_2	1.2	14.3	15.6	1.04	0.165
C_2H_2	1.0	12.0	11.4	0.98	0.171

The experimental conditions for both molecules are listed in Table I. The femtosecond laser wavelength is 0.8 μm . The maximum classical kinetic energy $2U_p$ of the direct electron signal is an indicator of the laser field strength in comparison with the ionization potential I_p of the molecule. Tunnel ionization requires Keldysh adiabaticity parameters $\gamma = [I_p/(2U_p)]^{1/2}$ lower or of the order of 1 [29]. In consequence, the used laser intensity is higher for N_2 , which has a higher ionization potential than C_2H_2 . The last parameter is the transverse momentum width σ_\perp from tunnel ionization, which will be introduced in Sec. II.

Finally this paper will not deal directly with strong-field photoelectron holography, a new physical effect discovered recently and coming from interferences between the direct and rescattered electron waves [30–35]. However, this important effect cannot be ignored for low-energy rescattered electron waves. Some of the main differences observed in N_2 and C_2H_2 will be attributed tentatively to a strong-field holographic signature in C_2H_2 .

The paper is organized as follows. Sec. II introduces some tools which are necessary for the analysis of the experimental data, and in particular the classical kinematics of rescattering. Indeed the kinematic momentum of the detected rescattered electron is not the momentum after the collision event as in experiments performed with electron beams. Therefore an introduction is necessary to establish the relationship between the measured quantities, denoted here as final momentum or equivalently final energy and final angle, with the physical quantities associated to the collision event and the laser field. We emphasize that this model can in no way replace a full quantum model for the interpretation of results and is developed only as a guide to the complex electron dynamics in strong laser fields. The experimental setup is presented in Sec. III and in particular the molecular alignment procedure which is required to reveal the effects of the potential anisotropy. The experimental results and their interpretation are discussed in Sec. IV with Secs. IV A to IV E devoted to the experimental results and the associated interpretations in N_2 and C_2H_2 about the direct and rescattered spectra.

II. GENERAL CONSIDERATIONS

Most of the kinematics of tunnel ionization and rescattering can be formulated classically in a linearly polarized laser field $\mathbf{F}(t) = \mathbf{e}_z F \cos(\omega t)$, assuming that the initial velocity of the electron immediately after tunnel ionization step is negligible [8]. The main contribution to ionization comes from

electron waves that have not been scattered by the ion core, i.e., the direct electron signal. For an electron tunneling at time t_0 and field phase $\varphi_0 = \omega t_0$, the final momentum p_{fz} at the end of the laser pulse along the polarization direction Oz is $p_{fz} = P \sin \varphi_0$ with $P = F/\omega$. Atomic units are used unless otherwise stated. The corresponding classical maximum energy is then twice the ponderomotive energy $2U_p = P^2/2 = (F/\omega)^2/2$.

Tunnel ionization models in a constant field \mathcal{F} developed in the 1960s showed that the dependence of the ionization rate on the transverse final momentum of the electron, $\mathbf{p}_{f\perp} = \mathbf{e}_x p_{fx} + \mathbf{e}_y p_{fy}$ exhibits a factor $\exp[-(\mathbf{p}_{f\perp}/\sigma_\perp)^2/2]$ with $\sigma_\perp^2 = \mathcal{F}/(2\kappa)$ where $\kappa = (2I_p)^{1/2}$ is the momentum associated to the ionization potential I_p [36]. Taking an ionization potential of 13.6 eV, an intensity of 10^{14} Wcm^{-2} at $0.8 \mu\text{m}$, we get $P/\sigma_\perp \simeq 6$ between the maximum final longitudinal momentum p_{fz} and the transverse momentum width σ_\perp , showing that tunnel ionization is peaked along the laser polarization.

In this paper, the direct electron spectrum is commented using the elegant model of Murray *et al.*, who showed that the electron spectrum may be written as a product of the squared modulus of the tunnel transition amplitude $a_t(F, \kappa, p_\perp)$ times the squared modulus of the partial Fourier transform $\phi(p_x, p_y, z_t)$ along the laser polarization transverse directions Ox and Oy of the initial wave function $\psi(x, y, z_t)$ [37]. The z_t coordinate is a tunneling coordinate along the laser polarization direction which has to be adjusted by fitting the ground state wave function with the WKB approximation of the tunneling wave function.

Rescattering is a second-order process and is therefore much less probable than direct ionization. Considering the recollision phase $\varphi_c = \omega t_c$ at time t_c when the electron revisits the ion core, the kinematic momenta \mathbf{p}_c^- , \mathbf{p}_c^+ , and \mathbf{p}_f , respectively, before the collision, after the collision, and at the end of the laser pulse, are given by

$$\mathbf{p}_c^- = \mathbf{e}_z P (\sin \varphi_0 - \sin \varphi_c), \quad (1)$$

$$\mathbf{p}_c^+ = \mathcal{R}(\Theta_c, \Phi_c)(\mathbf{p}_c^-), \quad (2)$$

$$\mathbf{p}_f = \mathbf{e}_z P \sin \varphi_c + \mathbf{p}_c^+, \quad (3)$$

where $\mathcal{R}(\Theta_c, \Phi_c)$ is the rotation of polar angle Θ_c and azimuthal angle Φ_c between the vectors \mathbf{p}_c^+ and \mathbf{p}_c^- defined in the collisional reference frame $Ox'y'z'$, where the component $p_{c,z'}$ along the Oz' axis of the collisional momentum \mathbf{p}_c^- before the collision is positive, i.e., $\mathbf{e}_{z'} = \mathbf{e}_z \times \text{sgn}(\sin \varphi_0 - \sin \varphi_c)$.

Classically, the recollision phase φ_c depends only on the ionization phase φ_0 and tunnel ionization coordinates of the electron. Assuming that tunnel ionization occurs at the origin, i.e., at the ion core, the relation linking φ_c to φ_0 is

$$\cos \varphi_c - \cos \varphi_0 + (\varphi_c - \varphi_0) \sin \varphi_0 = 0. \quad (4)$$

The return phase φ_c is then a multivalued function of the ionization phase φ_0 because of the multiple returns of the quivering electron. In consequence, the collision energy $E_c(\varphi_0) = [\mathbf{p}_c^-]^2/2 = [\mathbf{p}_c^+]^2/2 = 2U_p(\sin \varphi_0 - \sin \varphi_c)^2$ depends only on the ionization phase φ_0 . Its maximum $3.17U_p$ occurs at $\varphi_0 = 18^\circ$ and first return at $\varphi_c = 251.9^\circ$. For initial

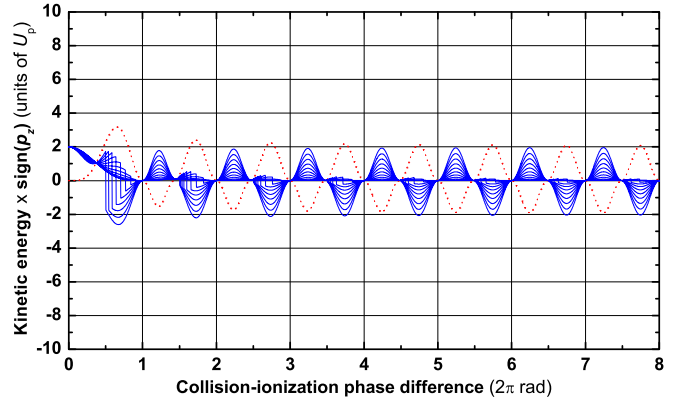


FIG. 1. Collision kinetic energy (red dotted line) and final kinetic energies (blue solid lines) as a function of the collision-ionization phase difference for different collision polar angles $\Theta_c \in [0^\circ, 60^\circ]$. The angle step of Θ_c is $\Delta\Theta_c = 6^\circ$. The kinetic energies are multiplied by the sign of the associated momentum component $p_z = \mathbf{p} \cdot \mathbf{e}_z$ where the unit vector \mathbf{e}_z points in the direction of the laser field at the ionization phase.

phases φ_0 such as $90^\circ \leq \varphi_0 < 180^\circ$ and $270^\circ \leq \varphi_0 < 360^\circ$, the electron does not revisit the core. Here we consider only initial phases $\varphi_0 \in [0^\circ, 90^\circ]$. Rescattering from initial phases $\varphi_0 \in [180^\circ, 270^\circ]$ may be deduced by symmetry inversion along the Oz axis.

Equations (1)–(3) establish the relationship between the collision angles Θ_c and Φ_c and the rescattering kinematics parameters $\{P = F/\omega, \sin \varphi_0, \sin \varphi_c\}$. However, there is not a one-to-one relationship between the measured final momentum \mathbf{p}_f and the collision physical quantities $\{\mathbf{p}_c^-, \Theta_c, \Phi_c\}$. Therefore in what follows, we will be interested in the dependence of the final momentum \mathbf{p}_f as a function of the laser phases φ_0 and φ_c and the collision polar angle Θ_c , since the azimuthal angle Φ_c , associated to the transverse momentum after the collision with respect to the laser field direction, is conserved *modulo* a frame adaptation between the laser frame $Oxyz$ and collision frame $Ox'y'z'$ with $\mathbf{e}_{z'} = \mathbf{e}_z \times \text{sgn}(\sin \varphi_0 - \sin \varphi_c)$. Since the return phase φ_c depends only on the ionization phase φ_0 because of the return condition Eq. (4), it is physically meaningful to introduce the phase difference $\varphi_{c0} = \omega(t_c - t_0) = \varphi_c - \varphi_0$. This phase denoted here collision-ionization phase difference is proportional to the time duration between tunnel ionization and recollision, i.e., the time spent by the electron in the continuum. In addition, it conveniently replaces the multivalued return phase $\varphi_c(\varphi_0)$. The final momentum \mathbf{p}_f is calculated from Eqs. (1)–(3) and the following equations giving $\sin \varphi_0$ and $\sin \varphi_c$ as a function of the collision-ionization phase difference φ_{c0} :

$$\sin \varphi_0 = (1 - \cos \varphi_{c0})f(\varphi_{c0}), \quad (5)$$

$$\sin \varphi_c = [-(1 - \cos \varphi_{c0}) + \varphi_{c0} \sin \varphi_{c0}]f(\varphi_{c0}), \quad (6)$$

where $f(x) = [2(1 - \cos x - x \sin x + x^2/2)]^{-1/2}$. These expressions are obtained from the electron return condition (4) and simple trigonometry calculations.

Figures 1–4 represent the final kinetic energy $E_f = \mathbf{p}_f^2/2$, final angle $\Theta_f = (\mathbf{e}_z, \mathbf{p}_f)$ defined in $[0^\circ, 180^\circ]$, and the final

experimental angle θ_f defined below, as a function of the phase difference φ_{c0} within four ranges of the collision polar angle Θ_c : $[0^\circ, 60^\circ]$, $[60^\circ, 90^\circ]$, $[90^\circ, 120^\circ]$, $[120^\circ, 180^\circ]$. These figures are not intended to give a precise knowledge of the final energy and angle, although available through Eqs. (1)–(6) but rather the ranges of these observables. The angle-energy representation instead of the momentum representation is chosen to conform to the electron angle-resolved energy spectra from the time-of-flight measurements. The collision kinetic energy and the final kinetic energy are represented as signed energies, i.e., $E_c \times \text{sgn}(p_{c,z}^-)$ and $E_f \times \text{sgn}(p_{f,z})$, respectively, including the sign of the component of the associated kinematic momentum with respect to the field unit vector \mathbf{e}_z . The calculation is performed for an initial phase $\varphi_0 \in [0^\circ, 90^\circ]$, and hence the laser electric field $\mathbf{F}(\varphi_0) = \mathbf{e}_z F \cos \varphi_0$ always points in the same direction at the ionization phase. Therefore the signed energy representation gives a straightforward account of the backward-forward directions of the different kinematic momenta with respect to the direction of the laser electric field direction and with respect to each other.

Figure 1 represents the signed collision kinetic energy and the final kinetic energy as a function of the collision-ionization phase difference for collision polar angles in the $[0^\circ, 60^\circ]$ range. The maximum of the collision energy $3.17U_p$ occurs at the first return with a phase difference lower than 2π rad. Then the local maxima tend towards $2U_p$ as the phase difference increases. This increase is associated to ionization phases φ_0 increasingly closer to zero. According to Eq. (1), the collision momentum \mathbf{p}_c^- tends towards $\mathbf{p}_c^- \simeq \mathbf{e}_z P \sin \varphi_{c0} \simeq \mathbf{e}_z P \sin \varphi_c$ giving the observed maxima and minima of the signed collision kinetic energy at $\pm P^2/2 = \pm 2U_p$. The collision kinetic energy is reported in Figs. 2–4 for comparison with the final kinetic energy.

The signed final kinetic energies in Fig. 1 are represented for 11 collision angles Θ_c from 0° to 60° with a step $\Delta\Theta_c = 6^\circ$. Jumps of the signed energies are observed from positive to negative values and *vice versa* because of the variation of the final angle Θ_f crossing the 90° limit between forward and backward directions with respect to the laser field direction at the ionization phase. The main conclusion of Fig. 1 is that the final kinetic energy remains approximately in the $[0, 2U_p]$ energy range dominated by the direct electron signal for collision angles smaller than 60° . While this feature is of importance for holography, it leads us to consider larger collision angles Θ_c to get smaller direct electron signals and smaller impact parameters.

In Figs. 2–4 we give the final experimental angle θ_f in addition to the final angle Θ_f which is calculated for an initial ionization phase $\varphi_0 \in [0^\circ, 90^\circ]$. This experimental angle is aimed at taking into account the ionization phase range $\varphi_0 \in [180^\circ, 270^\circ]$ and our single side time-of-flight spectrometer collecting electrons in the Ozx plane with $z \geq 0$ by convention (see Sec. III). From simple symmetry arguments, the final experimental angle is simply $\theta_f = \Theta_f$ when $\Theta_f \leq 90^\circ$ and $\theta_f = 180^\circ - \Theta_f$ when $\Theta_f > 90^\circ$. The restriction of θ_f to the $[0^\circ, 90^\circ]$ range results from the fact that we deal with symmetric molecules N_2 and C_2H_2 which are aligned along the Oz axis (parallel alignment to the laser field) or along the Ox axis (perpendicular alignment). Let us recall here that the positive and negative oscillations of the laser field with respect

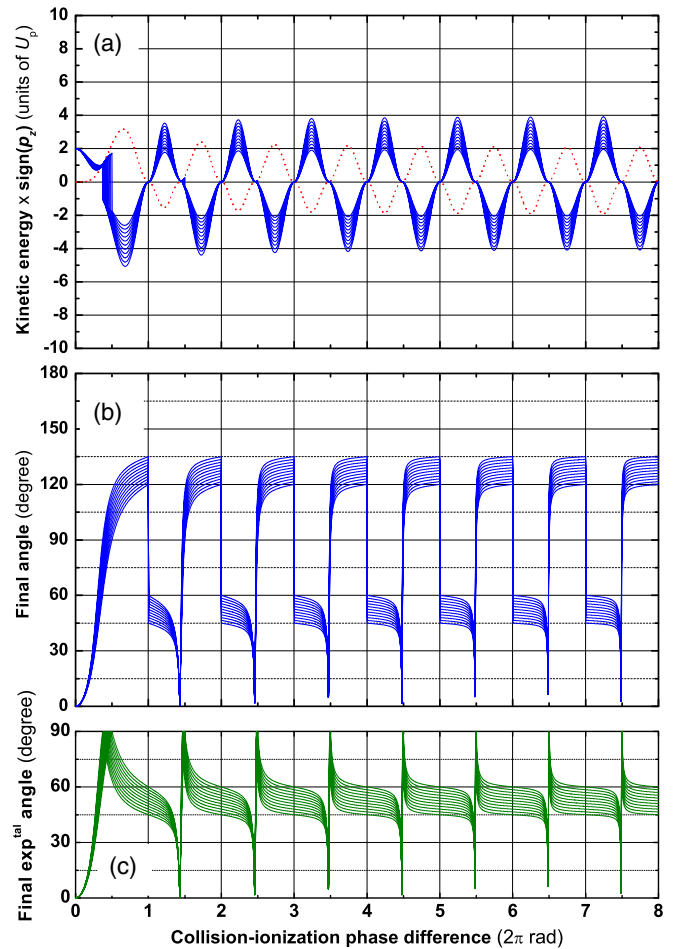


FIG. 2. Collision kinetic energy, final kinetic energies, final angle, and final experimental angle as a function of the collision-ionization phase difference for different collision polar angles $\Theta_c \in [60^\circ, 90^\circ]$. The angle step of Θ_c is $\Delta\Theta_c = 3^\circ$. (a) Collision kinetic energy (red dotted line), final kinetic energies (blue solid lines). The kinetic energies are multiplied by the sign of the associated momentum component $p_z = \mathbf{p} \cdot \mathbf{e}_z$ where the unit vector \mathbf{e}_z points in the direction of the laser field at the ionization phase. (b) Final angle $\Theta_f = (\widehat{\mathbf{e}_z}, \widehat{\mathbf{p}_f})$ (blue solid lines) where \mathbf{p}_f is the final momentum. (c) Final experimental angle θ_f (green solid lines) defined in the text and taking into account the indistinguishable positive and negative oscillations of the laser field and the molecular symmetries.

to \mathbf{e}_z are indistinguishable for a laser pulse of duration 40 fs at $0.8 \mu\text{m}$.

The signed final kinetic energies are presented in Fig. 2(a), Fig. 3(a), and Fig. 4(a) for the collision angle ranges $[60^\circ, 90^\circ]$, $[90^\circ, 120^\circ]$, and $[120^\circ, 180^\circ]$, respectively, with the signed collision kinetic energy which has been presented in Fig. 1. For each collision angle range, the maximum kinetic energy occurs at the first return with a collision-ionization phase difference smaller than 2π rad. In particular the maximum kinetic energy $10U_p$ is observed in Fig. 4(a) for a collision angle $\Theta_c = 180^\circ$. Except for collision-ionization phase differences smaller than π rad corresponding to kinetic energies lower than $2U_p$, the signed collision kinetic energy and the signed final kinetic energy have opposite signs. It means that the associated final momenta \mathbf{p}_f form an angle

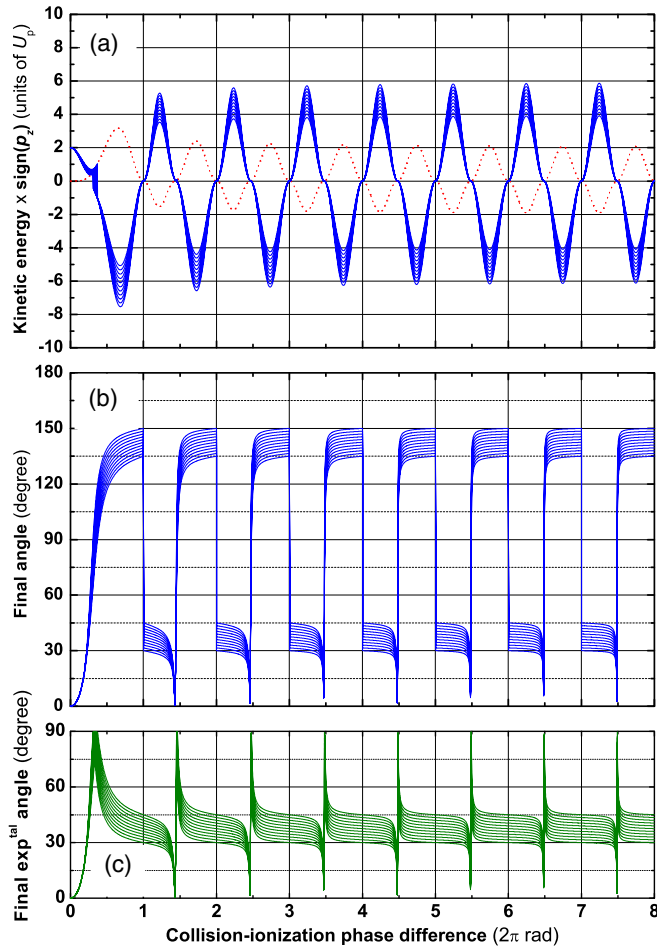


FIG. 3. Collision kinetic energy, final kinetic energies, final angle, and final experimental angle as a function of the collision-ionization phase difference for different collision polar angles $\Theta_c \in [90^\circ, 120^\circ]$. The angle step of Θ_c is $\Delta\Theta_c = 3^\circ$. (a) Collision kinetic energy (red dotted line), final kinetic energies (blue solid lines). The kinetic energies are multiplied by the sign of the associated momentum component $p_z = \mathbf{p} \cdot \mathbf{e}_z$ where the unit vector \mathbf{e}_z points in the direction of the laser field at the ionization phase. (b) Final angle $\Theta_f = (\hat{\mathbf{e}}_z, \hat{\mathbf{p}}_f)$ (blue solid lines) where \mathbf{p}_f is the final momentum. (c) Final experimental angle θ_f (green solid lines) defined in the text and taking into account the indistinguishable positive and negative oscillations of the laser field and the molecular symmetries.

with the collision incident momenta \mathbf{p}_c^- larger than 90° . This behavior is observed even for collision angles smaller than 90° in Fig. 2(a). As the collision-ionization phase difference increases, the local maxima and minima of the signed kinetic energies evolve to limit values with the same absolute values corresponding to the same values of the final kinetic energy. For the collision angle ranges $[60^\circ, 90^\circ]$ [Fig. 2(a)], $[90^\circ, 120^\circ]$ [Fig. 3(a)], and $[120^\circ, 180^\circ]$ [Fig. 4(a)], the limits of the maxima of the final kinetic energy $E_{f,\max}$ are given by the intervals $[2U_p, 4U_p]$, $[4U_p, 6U_p]$, and $[6U_p, 8U_p]$, respectively. In any case including relative small collision-ionization phase differences, these maxima are larger than $2U_p$ and take place in the energy range of the well-documented rescattering plateau [7,8].

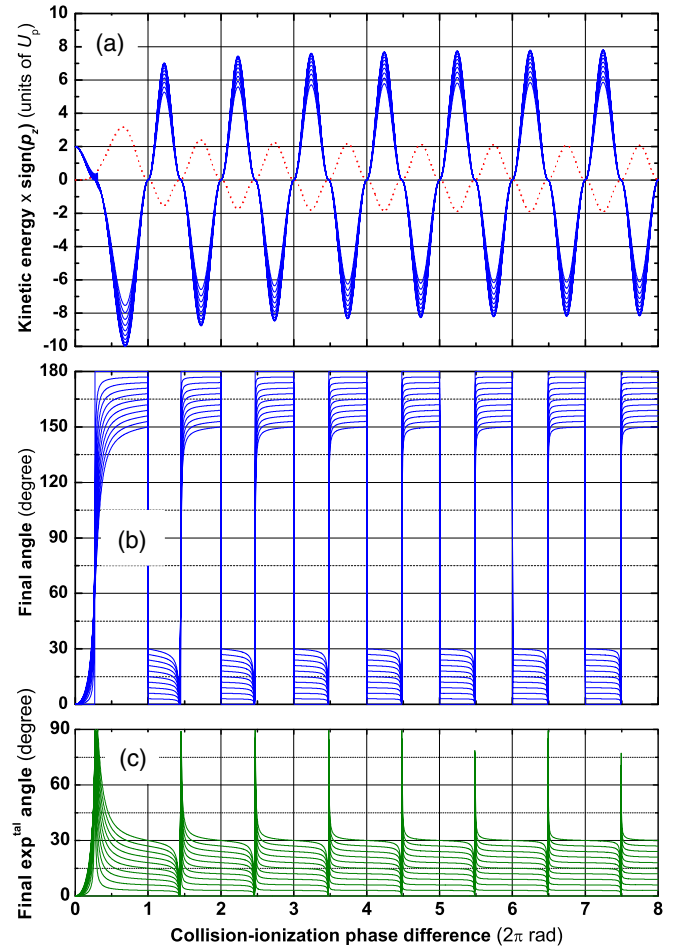


FIG. 4. Collision kinetic energy, final kinetic energies, final angle, and final experimental angle as a function of the collision-ionization phase difference for different collision polar angles $\Theta_c \in [120^\circ, 180^\circ]$. The angle step of Θ_c is $\Delta\Theta_c = 6^\circ$. (a) Collision kinetic energy (red dotted line), final kinetic energies (blue solid lines). The kinetic energies are multiplied by the sign of the associated momentum component $p_z = \mathbf{p} \cdot \mathbf{e}_z$ where the unit vector \mathbf{e}_z points in the direction of the laser field at the ionization phase. (b) Final angle $\Theta_f = (\hat{\mathbf{e}}_z, \hat{\mathbf{p}}_f)$ (blue solid lines) where \mathbf{p}_f is the final momentum. (c) Final experimental angle θ_f (green solid lines) defined in the text and taking into account the indistinguishable positive and negative oscillations of the laser field and the molecular symmetries.

The final angles and final experimental angles are presented in Figs. 2(b) and 2(c), Figs. 3(b) and 3(c), and Figs. 4(b) and 4(c) for the same ranges of the collision polar angle Θ_c as before. Discontinuity jumps of the final angles in Fig. 2(b), Fig. 3(b), and Fig. 4(b) correspond to passages from backward to forward electron emission and *vice versa* with respect to the laser field direction at the ionization phase. For each range of collisional angle, the final angle dependence reflects what is observed with the signed collision and final kinetic energies in Figs. 2(a), 3(a), and 4(a), respectively. As for kinetic energies, the final angle ranges evolve from their values when the phase difference is smaller than 2π rad to a stabilized pattern when the collision-ionization phase difference becomes large. The limit ranges of the final angle and final experiment angle are closely related. It is sufficient to mention the limit ranges of

TABLE II. Limit ranges of the maximum final kinetic energy $E_{f,\max}$, final angle Θ_f , and final experimental angle θ_f as a function of the range of the collision polar angle Θ_c when the difference between the rescattering phase and the ionization phase becomes large, i.e., larger than several times 2π rad.

Θ_c (degree)	$E_{f,\max}$ (U_p)	Θ_f (degree)	θ_f (degree)
[0, 60]	[0, 2]	[60, 90], [90, 120]	[60, 90]
[60, 90]	[2, 4]	[45, 60], [120, 135]	[45, 60]
[90, 120]	[4, 6]	[30, 45], [135, 150]	[30, 45]
[120, 180]	[6, 8]	[0, 30], [150, 180]	[0, 30]

the final experimental angles which are $[45^\circ, 60^\circ]$, $[30^\circ, 45^\circ]$, and $[0^\circ, 30^\circ]$ for the following ranges of the collision angle $[60^\circ, 90^\circ]$, $[90^\circ, 120^\circ]$, and $[120^\circ, 180^\circ]$, respectively.

The limit ranges of the maximum final kinetic energy, final angle and final experimental angle as a function of the range of the collision angle are listed Table II and correspond to collision-ionization phase differences larger than several times 2π rad. The limit values of Table II can be retrieved from Eqs. (1)–(3). When the collision-ionization phase difference φ_{c0} becomes large, i.e., $\varphi_0 \simeq 0$ and $\varphi_{c0} \simeq \varphi_c$, the final angle and kinetic energy are given, respectively, by

$$\Theta_f = [\pi - \Theta_c \times \text{sgn}(\sin \varphi_c)]/2, \quad (7)$$

$$E_f = 8U_p \sin^2(\Theta_c/2) \sin^2(\varphi_c). \quad (8)$$

Equations (7) and (8) give the limit values reported in Table II taking $\varphi_c = (k + 1/2)\pi$ rad with k being an integer.

Although smaller collision-ionization phase differences than 2π rad are of importance, these limit ranges allow us to draw some useful conclusions about the detected electron angle-resolved energy spectra. The first one is that the collisional angle range below 60° is reachable only using holography since the final energy range approximately below $2U_p$ takes place in the energy range of the direct electron emission. Differential cross sections of elastic scattering are large for small scattering angles following the trend of the well-known Rutherford cross section. In consequence, holography was shown to play an important role in this final energy range although rescattering is a second-order process compared to direct ionization [30–35]. For our purpose, small collision angles are associated to large impact parameters which do not favor the probe of the short-range anisotropic potential as it is outlined in Sec. I.

It can be inferred from Figs. 2(c)–4(c) and Table II that the final experimental angle decreases as the maximum final kinetic energy increases. From the above equations it is possible to get the maximum final experimental angle $\theta_{f,\max}$ as a function of the final kinetic energy E_f . Let us mention that the minimum final experimental angle $\theta_{f,\min}$ is always 0° since final energies vary from zero to their maximum values and in particular for the collision angle range $[120^\circ, 180^\circ]$. Figures 5(a) and 5(b) presents the dependence of $\theta_{f,\max}$ as a function of E_f for large collision-ionization phase differences and for all collision-ionization phase differences, respectively. For large return phase differences, this dependence is given

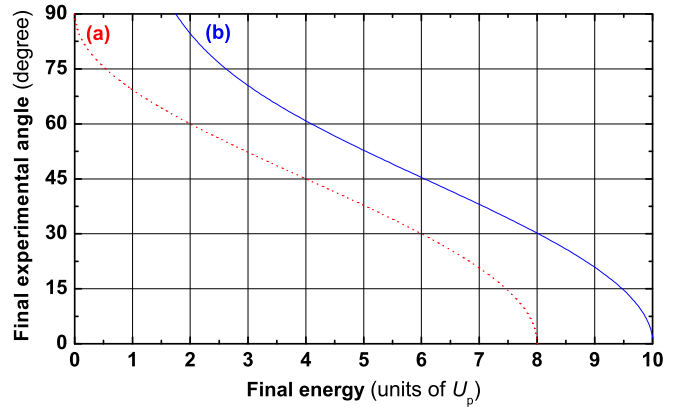


FIG. 5. Largest experimental angle $\theta_{f,\max}$ as a function of the final energy. (a) (red dotted line): For large collision-ionization phase differences, i.e., larger than several times 2π rad. (b) (blue solid line): For all collision-ionization phase differences.

by Eqs. (7) and (8) taking $\varphi_c = (k + 1/2)\pi$ with k being an integer:

$$\theta_{f,\max} = \arccos \{ [E_f / (8U_p)]^{1/2} \}. \quad (9)$$

The maximum final experimental angle is given by the first return and is reported in Fig. 5(b) as a function of the final energy. The increases in comparison with large phase differences are around 25° at $2U_p$, 15° at $4U_p$ and $6U_p$, and 30° at $8U_p$. Interestingly, we reproduce the maximum final angle range presented in Fig. 5(b) with quantum calculations based on the strong-field approximation theory (SFA) and taking a Born approximation for the rescattering matrix element with a model potential. The reason for the agreement with the classical model is the absence of the ion Coulomb potential experienced by the quivering electron since we took the basic version of SFA where the rescattering waves are plane waves. See, for instance, Refs. [8–10] for the different versions of SFA. In addition, the free quantum diffusion of the rescattering wave packet in the transverse dimensions with respect to the laser polarization direction, strongly favors the first return in terms of rescattering flux.

From an experimental point of view, large angular widths give a better chance to observe a potential anisotropy than small angular widths because of the extended range of angular detection. However, small final experimental angles correspond to large collision angles associated to small impact parameters best suited for probing a short-range potential. Therefore we will experiment a tradeoff between detection efficiency and physical efficiency of the short-range potential probe.

As a final remark, let us emphasize that the above classical model represents an over-simplified description of rescattering since it describes only the classical dynamics of the electron in the laser field without any molecular ionic potential. In addition to its limitation in the classical domain, the intrinsically quantum nature of scattering involves a multielectronic dynamics at collision energies of a few tens of electronvolts. Therefore we consider this kinematic model as a guide for the interpretation of the experimental data, but definitely not a valuable framework for qualitative and

quantitative interpretations. To our opinion, this statement justifies the needs for experimental data due to the formidable task represented by the developments of numerical codes aimed at solving the time-dependent Schrödinger equation in strong laser fields involving a multielectronic dynamics.

III. EXPERIMENTAL SETUP

Laser-induced impulsive alignment is used to obtain spatially aligned molecular samples in free-field conditions [38–40]. A linearly polarized laser pulse with duration much smaller than the molecular rotational period encodes coherences between the rotational levels. Picoseconds later after the end of the laser pulse, the revivals of the resulting rotational wave packets lead to transient spatial alignments for a few hundreds of femtoseconds at fractional times of the Raman rotational period $(2cB_0)^{-1}$, where c is the speed of light and B_0 the rotational constant in wave number units. The second probe ionizing pulse is delayed with respect to the pump alignment pulse, when the alignment along the pump polarization is maximal.

The alignment setup as well as the photoelectron time-of-flight detection have been presented elsewhere [41]. In brief, a 3 kHz titanium-sapphire laser system delivering pulses of duration 40 fs and energy 0.7 mJ at 0.8 μm is used to produced pump-alignment pulses with intensities of the order of 10^{13} Wcm^{-2} and probe-ionization pulses in the 10^{14} Wcm^{-2} range. The pump pulses are stretched to 120 fs in order to improve the alignment while keeping the intensity sufficiently low in order to avoid any ionization event [40]. The pump and probe pulses are separated in a Michelson-type interferometer, where a zero-order half-wave plate in the pump arm is aimed at choosing the alignment direction parallel or perpendicular to the ionizing pulse polarization.

After recombination, the pump and probe pulses are sent in the high-vacuum chamber housing the on-axis focusing parabolic mirror, a short ion 140 mm time-of-flight ion spectrometer and a long 700 mm time-of-flight electron spectrometer, on both sides of the laser focus. The temperature of the supersonic expansion is estimated from fits of the experimental ion revivals with calculations from tunnel ionization and alignment distributions to 50 K in N_2 and 30 K in C_2H_2 [40].

The photoelectrons are collected in a cone of apex angle 3° by microchannel plates. The conversion from time of flight to kinetic energy E_f gives an energy resolution ΔE_f scaling as $E_f^{3/2}$, and being 50 meV at 10 eV and 1.6 eV at 100 eV owing the 0.5 ns time bin of the digitizer. The photoelectron angle-resolved energy spectra from 0 to 90° with respect to the laser polarization are recorded by turning a zero-order half wave plate which rotates the pump and probe polarizations with respect to the detection time-of-flight axis. The wave plate is continuously rotated with a step of 1° . At each step, the time-of-flight spectrum is averaged over 30 000 laser shots. The recording is stopped when we get of the order of 10^6 shots per angle. The angle between the laser polarization and the time-of-flight axis corresponds to the final experimental angle θ_f defined in Sec. II and is denoted final angle from now on.

The electrons are detected in the wavefront plane Ozx , where Oz is along the laser polarization direction following

our convention in Eqs. (1)–(3). In consequence, the transverse momenta p_{fy} of the detected electrons along the propagation direction Oy are zero, i.e., $p_{fy} = 0$ [41]. Taking into account that $(p_{fz}, p_{fx}) = (2E_f)^{1/2}(\cos \theta_f, \sin \theta_f)$ where E_f is the measured final energy from the time of flight and θ_f the final angle between the laser polarization and time-of-flight axis, we have $S(E_f, \theta_f) = S_{\mathbf{p}_f}(p_{fz}, p_{fx})$ between the angle-resolved energy spectrum and the momentum spectrum since the Jacobian $|\partial(p_{fz}, p_{fx})/\partial(E_f, \theta_f)| = m_e = 1$ atomic unit, where m_e is the electron mass. In the hereinafter referred parallel and perpendicular alignments, molecules are aligned along the Oz axis, i.e., the laser polarization direction, and the along Ox axis, respectively. As it is outlined in Sec. II, it is sufficient to vary θ_f from 0° to 90° because of the indistinguishable positive and negative oscillations of the laser light along the laser polarization direction Oz and the symmetric character of N_2 and C_2H_2 along the alignment axes Oz or Ox .

The angular distributions with final energies above $2U_p$ present structureless bell-shaped profiles with maxima at 0° . Since the spectra from parallel and perpendicular alignments do not drastically differ, these spectra are compared using two functions depending only on energy, and denoted the angle-integrated energy spectrum $S_i(E_f)$ and the angular width $\Theta_i(E_f)$. The angle-integrated energy spectrum $S_i(E_f)$ is defined by

$$S_i(E_f) = \int_0^{\pi/2} S(E_f, \theta_f) d\theta_f. \quad (10)$$

The angular width $\Theta_i(E_f)$ is defined by

$$S_i(E_f) = 2 \int_0^{\Theta_i(E_f)} S(E_f, \theta_f) d\theta_f, \quad (11)$$

and is the final angle for which the angular cumulative distribution from 0° to this angle is half the angular cumulative distribution from 0° to 90° at E_f , i.e., $S_i(E_f)$. In the following Sec. IV, parallel and perpendicular alignments are compared using the ratio of angle-integrated spectra and the ratio of angular widths as a function of the final energy. These ratios come from the corresponding values measured in perpendicular alignment divided by the same values measured in parallel alignment, all other experimental conditions being equal.

IV. RESULTS AND DISCUSSION

A. Photoelectron angle-resolved energy spectra in N_2 and C_2H_2

Figure 6 presents the photoelectron angle-resolved energy spectra recorded with N_2 and C_2H_2 in parallel and perpendicular alignments with a final angle $\theta_f = 0^\circ$. As expected from previous studies, these molecules exhibit an opposite behavior: The ionization of N_2 (C_2H_2) is favored in parallel (perpendicular) configuration thus emphasizing the role of the HOMO symmetry and geometry in the tunnel ionization process [25,27,41]. The $2U_p$ classical limits of the energy of direct electron signals are indicated in Fig. 6. As it was reported by many authors and owing the simplistic approach of the classical model, these limits do not occur at energies corresponding to the visual separation with the rescattered electron plateau because of quantum effects. See for instance the calculated spectra in Refs. [12,13]. Although the laser

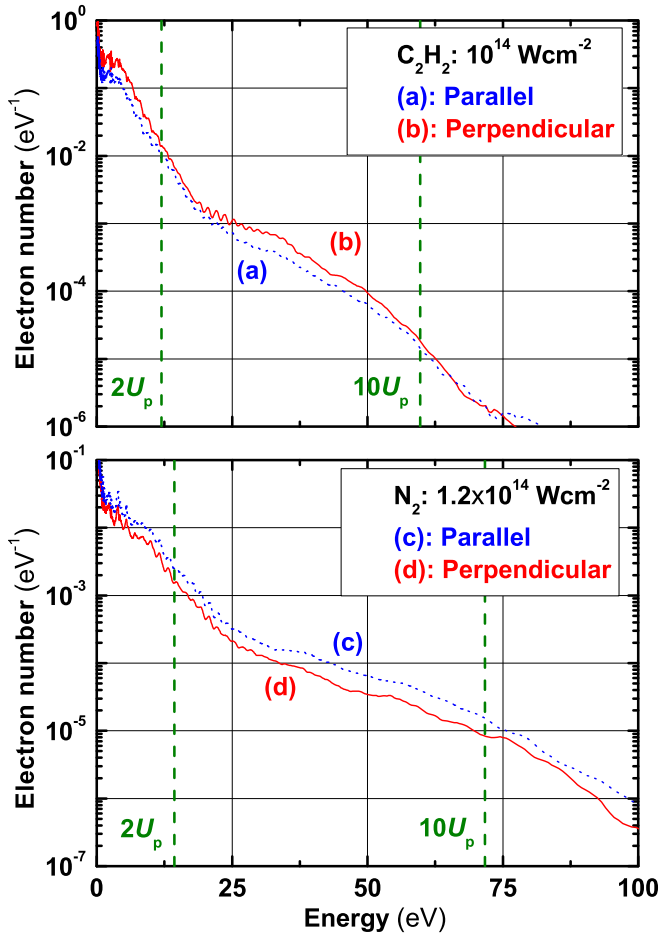


FIG. 6. Photoelectron angle-resolved energy spectra recorded at $0.8 \mu\text{m}$ with the laser polarization parallel to the time-of-flight axis, i.e., $\theta = 0^\circ$. Top panel: C_2H_2 at 10^{14} Wcm^{-2} . (a) (blue dotted line): Parallel alignment. (b) (red solid line): Perpendicular alignment. Bottom panel: N_2 at $1.2 \times 10^{14} \text{ Wcm}^{-2}$. (c) (blue dotted line): Parallel alignment. (d) (red solid line): Perpendicular alignment. The classical energy limits at $2U_p$ and $10U_p$ are indicated by vertical green dashed lines.

intensity was slightly increased from 10^{14} to $1.2 \times 10^{14} \text{ Wcm}^{-2}$ in N_2 in order to get a similar Keldysh adiabaticity parameter $\gamma \simeq 1$, the electron signals remain lower in N_2 than in C_2H_2 because of the higher ionization potential $I_p(\text{N}_2) = 15.6 \text{ eV}$ of N_2 compared to $I_p(\text{C}_2\text{H}_2) = 11.4 \text{ eV}$ [42,43]. However, the comparison between both gases is not straightforward because of the different gas densities in the supersonic expansions. The photonic separation of above-threshold ionization peaks appears up to $\sim 30 \text{ eV}$ due to the increased energy resolution at low energies for long times of flight. The peaks are broadened by the laser field and Freeman resonances which are resolved at very low energy [44]. These multiphotonic resonances are out the scope of this report and will be analyzed in a future work.

Finally, the decrease of the rescattering plateau beyond the $10U_p$ limit is more pronounced in C_2H_2 than in N_2 . This behavior is observed at other laser intensities. To our knowledge, scattering differential cross sections are not available in the

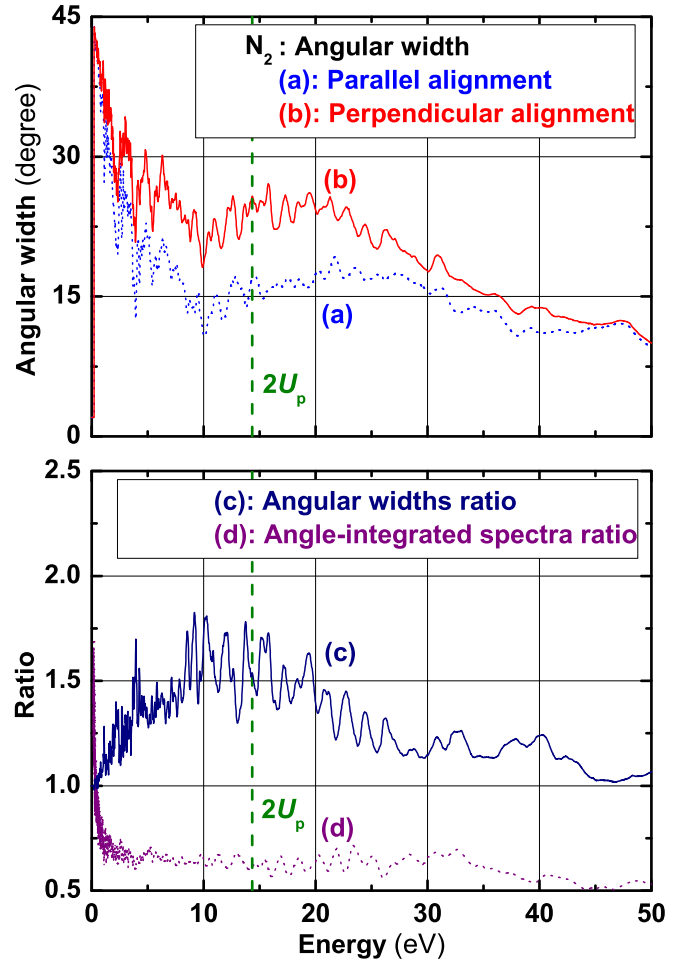


FIG. 7. Top panel: Angular widths recorded in N_2 at $1.2 \times 10^{14} \text{ Wcm}^{-2}$. (a) (blue dotted line): Parallel alignment. (b) (red solid line): Perpendicular alignment. Bottom panel: Ratios of the angular widths and angle-integrated energy spectra in N_2 from angle-resolved energy spectra recorded in perpendicular and parallel alignments, respectively. (c) (navy solid line): Ratio of the angular widths. (d) (purple dotted line): Ratio of the angle-integrated energy spectra. The classical energy limit at $2U_p$ of the direct electron signal is indicated by vertical green dashed lines.

case of electron-cation elastic scattering for these molecules at collision energies in the 20 eV range. Therefore the respective strong field and molecular contributions to this experimental fact remain difficult to disentangle.

B. Direct electron spectra in N_2

The angular widths from the spectra recorded in N_2 in parallel and perpendicular alignments are presented in the top panel of Fig. 7. For both alignments, a steep decrease is observed as a function of the final energy from 0 to 10 eV . This is due to the sole contribution of the direct electron signal which strongly dominates the overall electron signal at these energies below $2U_p$. The steep decrease is common to parallel and perpendicular alignments and come from the tunnel amplitude of direct ionization. Introducing the dimensionless final energy parameter $\mathcal{E}_f = E_f/(2U_p)$ and the final angle θ_f in the tunnel amplitude a_t of Murray *et al.* [37],

we get

$$|a_t|^2 \propto \frac{1}{(1 - \mathcal{E}_f \cos^2 \theta_f)^{1/\kappa+1/2}} \times \exp \left[-\frac{2\kappa^3}{3F} \frac{1 + (3/2)\gamma^{-2}\mathcal{E}_f \sin^2 \theta_f}{(1 - \mathcal{E}_f \cos^2 \theta_f)^{1/2}} \right], \quad (12)$$

where the factors not depending on \mathcal{E}_f and θ_f have been dropped, and where the normalization to final energy and angle has been applied. The tunnel amplitude a_t is expressed in atomic units where γ is the Keldysh parameter introduced in Sec. I and Table I and $\kappa = (2I_p)^{1/2}$ is the electron momentum associated to the ionization potential introduced in Sec. II. In Eq. (12) the dependence $\exp[-(\mathbf{p}_{f\perp}/\sigma_\perp)^2/2]$ introduced in Sec. II of the transverse momentum distribution appears as $\exp[-(\kappa/\gamma)^2(\kappa/F)\mathcal{E}_f \sin^2 \theta_f/(2U_p)]$, and is responsible for the strong decrease of the angular width of the direct electron spectrum as the final energy E_f increases, since this factor is $\exp[-18.3\mathcal{E}_f \sin^2 \theta_f/(2U_p)]$ assuming a single laser intensity at $1.2 \times 10^{14} \text{ Wcm}^{-2}$. The modulations in the angular width are due to photonic above-threshold ionization structures since the ionization process is repeated over many cycles of the pulse.

In Fig. 7 the angular width is smaller for parallel alignment than for perpendicular alignment in N_2 . The bottom panel shows the ratio of the angular widths [Fig. 7(c)] between the perpendicular and parallel configurations. As expected from Figs. 7(a) and 7(b), this ratio is larger than 1. It increases from 1 to ~ 1.7 as the energies increases from 0 to 10 eV. This energy range mainly receives the contribution of the direct electron signal, and in consequence this increase has to be searched in the dependence of this signal with the molecular alignment, i.e., the initial molecular wave function prior to tunnel ionization. Following our $Oxyz$ axes convention, the HOMO $3\sigma_g$ of N_2 may be represented in parallel configuration along the Oz axis as the difference of two $2p_z$ atomic wave functions, spatially shifted by the equilibrium internuclear distance R_e . The same argument holds for molecules aligned along the Ox axis in perpendicular alignment with $2p_x$ atomic wave functions instead of $2p_z$ orbitals.

Following Murray *et al.*, the final electron spectrum is proportional to $|a_t|^2 |\phi(p_{fx}, p_{fy}, z_t)|^2$, where $\phi(p_{fx}, p_{fy}, z_t)$ is the partial Fourier transform along the transverse directions Ox and Oy of the ground state wave function, and z_t is the WKB fitting distance. The wave functions $\psi_{3\sigma_{g,\parallel}}(x, y, z)$ and $\psi_{3\sigma_{g,\perp}}(x, y, z)$, and the squared moduli of their partial Fourier transforms $|\phi_{3\sigma_{g,\parallel}}(p_{fx}, p_{fy}, z_t)|^2$ and $|\phi_{3\sigma_{g,\perp}}(p_{fx}, p_{fy}, z_t)|^2$ in parallel and perpendicular alignments are, respectively,

$$\psi_{3\sigma_{g,\parallel}}(x, y, z) \propto \psi_{\text{at},p_z}(x, y, z - R_e/2) - \psi_{\text{at},p_z}(x, y, z + R_e/2), \quad (13)$$

$$\psi_{3\sigma_{g,\perp}}(x, y, z) \propto \psi_{\text{at},p_x}(x - R_e/2, y, z) - \psi_{\text{at},p_x}(x + R_e/2, y, z), \quad (14)$$

$$|\phi_{3\sigma_{g,\parallel}}(p_{fx}, p_{fy}, z_t)|^2 \propto \exp[-(p_{fx}^2 + p_{fy}^2)/\alpha], \quad (15)$$

$$|\phi_{3\sigma_{g,\perp}}(p_{fx}, p_{fy}, z_t)|^2 \propto [p_{fx} \sin(p_{fx}R_e/2)]^2 \times \exp[-(p_{fx}^2 + p_{fy}^2)/\alpha], \quad (16)$$

where $\alpha = \kappa/|z_t|$, and $\psi_{\text{at},p_x}(x, y, z)$ and $\psi_{\text{at},p_z}(x, y, z)$ are the $2p_x$ and $2p_z$ atomic wave functions, respectively, expressed in the laboratory $Oxyz$ frame. Equations (15) and (16) are established assuming that the transverse coordinates x and y of the wave function are small in comparison with the tunneling coordinate z_t . In that case, the radial dependence $\exp(-\kappa r)$ with $r = (x^2 + y^2 + z_t^2)^{1/2}$ of the $2p$ atomic orbitals is replaced by a Gaussian function of x and y since $r \simeq |z_t| + (x^2 + y^2)/(2|z_t|)$.

In Eq. (16) the prefactor before the Gaussian momentum dependence in exhibits a $p_{fx}^4 = (2E_f \sin^2 \theta_f)^2$ dependence since $p_{fx}R_e/2 \ll 1$. The equality $p_{fx}R_e/2 = 1$ with p_{fx} and R_e in atomic units gives a transverse energy $p_{fx}^2/(2m_e) \simeq 15 \text{ eV}$, which is much larger than the measured transverse energies. Recalling that $p_{fy} = 0$ in our experiments, the factor $(2E_f \sin^2 \theta_f)^2$ is responsible for a larger angular width of the direct electron spectrum in the perpendicular alignment for N_2 . A numerical simulation taking into account Eqs. (12), (15), and (16) shows that the ratio of the angular widths between perpendicular and parallel alignments increases as the energy increases as it is observed in Fig. 7. This behavior when the energy increases from 0 eV in the exponential factor $\exp[-aE_f \sin^2(\theta_f)]$ where a is a constant, is due to the prefactor $\sin^4(\theta_f)$ which draws the angular distribution to large angles in perpendicular alignment. A numerical comparison with the experimental data although in some cases satisfactory, is not realistic because the alignment distributions are not known, and Eqs. (12)–(16) are valid for a single laser intensity or maximum field amplitude F while our experiments include the intensity distribution in the laser focus. In particular, the WKB fitting distance z_t does depend on F [37].

Finally following Eq. (16) and the above discussion, no direct electron signal is expected in perpendicular alignment when $p_{fx} = 0$, i.e., when the final angle $\theta_f = 0^\circ$ in sharp disagreement with the spectrum of Fig. 6(d) recorded at $\theta_f = 0^\circ$. The first reason of this disagreement is the over-simplified model of the $3\sigma_g$ HOMO of N_2 using only one $2p$ atomic orbital per nitrogen atom. More sophisticated models show that the tunnel ionization rate of the HOMO of N_2 exhibits a bell-shaped dependence as a function of the angle between the laser polarization direction and the molecular axis with the maximum at 0° and the minimum at 90° [26,45,46]. However, the predicted ratio between the rates in perpendicular and parallel alignments is weaker than what is observed here. The main reason comes from the rather broad angular distributions of the molecular axis around the chosen directions using impulsive alignment. For instance, Meckel *et al.* and Walt *et al.* in their study of strong-field holography use normalized differences of photoelectron momentum distributions recorded at different alignment conditions to reveal holographic patterns [34,35]. In general, angular distributions of the molecular axis lead to moderate contrasts between photoelectron spectra recorded at the desired different alignments and different strategies are necessary to recover the alignment dependence. In what follows, this is the reason why we use ratios between the angular widths $\Theta_i(E_f)$ and angle-integrated energy spectra $E_i(E_f)$ defined in Sec. III recorded at perpendicular and parallel alignments, respectively.

C. Rescattered electron spectra in N_2

In Figs. 7(a) and 7(b), the angular widths stop decreasing at 10 eV below $2U_p$, increase again up to ~ 20 eV above $2U_p$ and then decrease again. The increase of the angular widths beginning at 10 eV is due to the rescattered electron signal since the angular width of the direct electron signal is expected to strongly decrease as the final energy increases. It should be emphasized that the electron signal between 10 eV and 20 eV is still higher than the plateau as it can be seen in Figs. 6(c) and 6(d). Therefore the increase of the angular widths as a function of energy beginning at 10 eV below $2U_p = 14.3$ eV (see Table I) constitutes a signature of the contribution of the rescattered electron signal to the total electron signal. Moreover the increases of the angular widths are due to the decreases of the direct electron signals. Considering now Table II, the final energy range below $2U_p$ correspond to collision angles smaller than 60° . The fact that small collision angles are associated to large scattering cross sections probably enhances the influence of rescattering below the $2U_p$, where the direct electron signal is dominant.

For energies larger than 20 eV, the direct electron signal does not contribute to the spectrum anymore, and the decrease of the angular width is only due to the rescattered electron signal. Considering Fig. 5(b), the final angle is expected to decrease as the final energy increases. The energy range above $2U_p$ of Fig. 7 spans from $2U_p$ to $7U_p$. The corresponding final angle ranges are much smaller than the maximum final angles reported in Fig. 5(b). Although the angular widths are cumulative widths defined in Eqs. (10) and (11) and taking into account that quantum values often extends beyond classical values, this difference is probably due to the absence of the Coulomb potential in the classical model of Sec. II.

In Fig. 7(d) the ratio of the angle-integrated energy spectra between perpendicular and parallel alignments remains almost constant and around 0.6 for energies in the range from 1 eV to 35 eV. In the range from 0 eV to 1 eV, we do not have any explanation for the surprising steep decrease of the ratio between the spectra. The passage from the direct electron spectrum to the rescattered one does not induce any significant change of this ratio. For energies lower than $2U_p$, this ratio is simply the efficiency ratio between both alignments for direct ionization. Considering that the total rescattered signal is the returning electron flux times the total scattering cross section and that the returning electron flux is proportional to the total ionization rate, the unchanging ratio shows that the total scattering efficiency does not significantly differ in parallel and perpendicular configurations.

The angular widths of the rescattered electron spectra in Figs. 7(a) and 7(b) remain different. The angular width recorded in perpendicular alignment is larger than the angular width recorded in parallel alignment. These curves as well as the ratio of the angular widths in Fig. 7(c) show that the difference is less pronounced when the final energy increases. Although the rescattered signals become very weak above 35 eV, the angular widths from parallel and perpendicular alignments tend to become closer, and their ratio approaches 1. As a first conclusion in N_2 , the angular width recorded from perpendicular alignment is larger than the angular width recorded from parallel alignment for both the direct and rescattered waves. Is this feature related to the

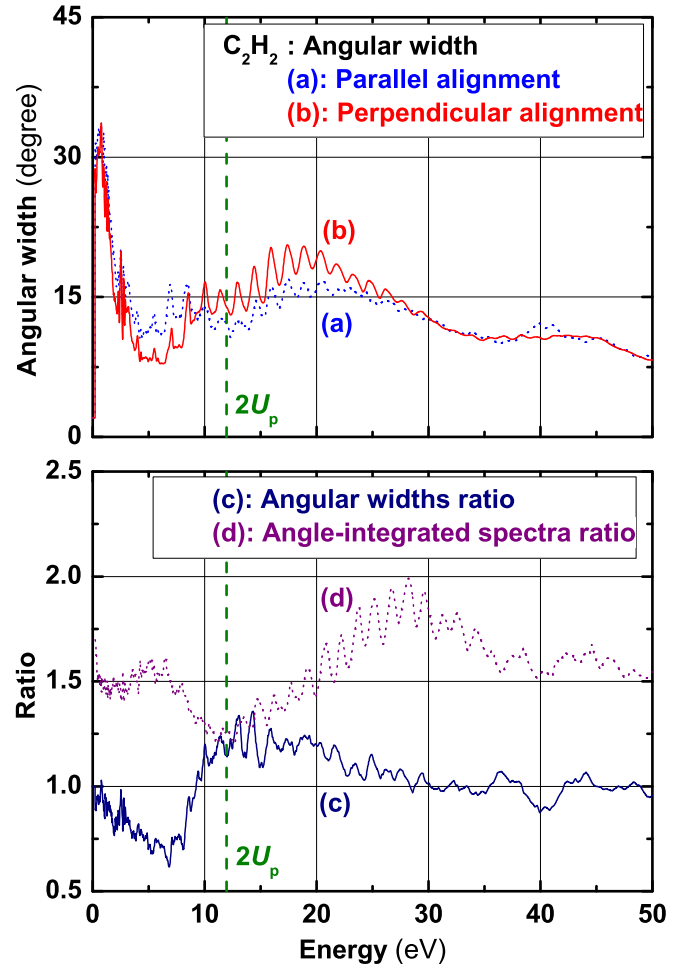


FIG. 8. Top panel: Angular widths recorded in C_2H_2 at 10^{14} Wcm^{-2} . (a) (blue dotted line): Parallel alignment. (b) (red solid line): Perpendicular alignment. Bottom panel: Ratios of the angular widths and angle-integrated energy spectra in C_2H_2 from angle-resolved energy spectra recorded in perpendicular and parallel alignments, respectively. (c) (navy solid line): Ratio of the angular widths. (d) (purple dotted line): Ratio of the angle-integrated energy spectra. The classical energy limit at $2U_p$ of the direct electron signal is indicated by vertical green dashed lines.

sole larger distribution from tunnel ionization? The answer will be given with C_2H_2 which exhibits an inverse behavior with respect to tunnel ionization and alignment. The second conclusion is that the difference of angular widths is more pronounced for relatively low final energy. This feature is common with C_2H_2 and other molecules and relies on small final angles as the final energy approaches and goes beyond the classical limit $10U_p$. Less angular space is then available for the observation of angular differences.

D. Direct electron spectra in C_2H_2

The angular widths from the spectra recorded in C_2H_2 are presented in Figs. 8(a) and 8(b). For both alignments, a steep decrease is observed as a function of the final energy from 0 up to $U_p = 6$ eV for both alignments. As for N_2 , this is due to the sole contribution of the direct electron signal and to

the tunnel amplitude of direct ionization discussed above with Eq. (12). The difference with N_2 in this energy range is that the width recorded in perpendicular alignment is smaller than the width recorded in parallel alignment. Moreover, considering Fig. 8(c), the ratio between the widths in perpendicular and parallel alignments now decreases as the energy increases from 0 to U_p while it increases in N_2 .

Although the behaviors are contrary in N_2 and C_2H_2 , they come from the same origin, i.e., the initial wave function appearing in the electron spectrum through the squared modulus $|\phi(p_{fx}, p_{fy}, z_t)|^2$ of its partial Fourier transform [37]. The HOMO $1\pi_u$ of C_2H_2 and more precisely its $1\pi_{ux}$ component, may be represented in parallel configuration as the sum of two $2p_x$ atomic orbitals spatially shifted by the bond distance R_e between the carbon nuclei. In perpendicular alignment, the $2p_x$ atomic orbitals have to be replaced by $2p_z$ atomic orbitals. Using the same approximations and notations as for N_2 , the corresponding wave functions $\psi_{1\pi_{ux,\parallel}}(x, y, z)$ and $\psi_{1\pi_{ux,\perp}}(x, y, z)$, and the squared moduli of their partial Fourier transforms $|\phi_{1\pi_{ux,\parallel}}(p_{fx}, p_{fy}, z_t)|^2$ and $|\phi_{1\pi_{ux,\perp}}(p_{fx}, p_{fy}, z_t)|^2$ in parallel and perpendicular alignments are, respectively,

$$\psi_{1\pi_{ux,\parallel}}(x, y, z) \propto \psi_{at,p_x}(x, y, z - R_e/2) + \psi_{at,p_x}(x, y, z + R_e/2), \quad (17)$$

$$\psi_{1\pi_{ux,\perp}}(x, y, z) \propto \psi_{at,p_z}(x - R_e/2, y, z) + \psi_{at,p_z}(x + R_e/2, y, z), \quad (18)$$

$$|\phi_{1\pi_{ux,\parallel}}(p_{fx}, p_{fy}, z_t)|^2 \propto p_{fx}^2 \exp[-(p_{fx}^2 + p_{fy}^2)/\alpha], \quad (19)$$

$$|\phi_{1\pi_{ux,\perp}}(p_{fx}, p_{fy}, z_t)|^2 \propto \cos^2(p_{fx}R_e/2) \times \exp[-(p_{fx}^2 + p_{fy}^2)/\alpha]. \quad (20)$$

Since $p_{fx}R_e/2 \ll 1$ and hence $\cos^2(p_{fx}R_e/2) \simeq 1$, the dependence of $|\phi_{1\pi_{ux,\perp}}(p_{fx}, p_{fy}, z_t)|^2$ is Gaussian in perpendicular alignment, while $|\phi_{1\pi_{ux,\parallel}}(p_{fx}, p_{fy}, z_t)|^2$ exhibits a p_{fx}^2 prefactor before the Gaussian in parallel alignment. Taking into account that $p_{fy} = 0$ in our experiments, this prefactor is responsible for the larger angular width in parallel configuration as well as for the decrease of the angular widths ratio as the energy is increased.

In other words, the node of the spatial wave function along the laser polarization direction in parallel alignment leads to a larger angular distribution. As for N_2 , a direct comparison with the experimental data would require a precise knowledge of the alignment distributions, a more realistic description of the HOMO, and finally an integration over the laser field within the focal volume.

Following Eq. (19), no direct electron signal is expected in parallel alignment when $p_{fx} = 0$, i.e., when the final angle $\theta_f = 0^\circ$ in disagreement with direct electron detection at a final angle $\theta_f = 0^\circ$ as in the case of perpendicular alignment of N_2 . The reason is here the same as for N_2 and is attributed to the used over-simplified model of the HOMO.

E. Rescattered electron spectra in C_2H_2

In Fig. 8(d) the ratio between the total electron signals recorded in C_2H_2 in perpendicular and parallel alignments

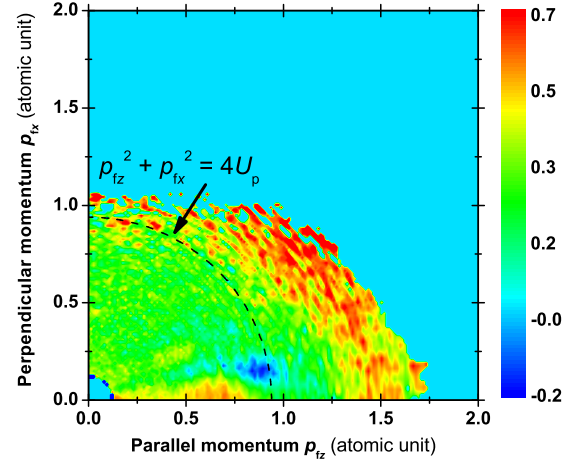


FIG. 9. Photoelectron normalized difference momentum spectrum $\Delta S_{pr}(p_{fz}, p_{fx})$ defined by Eq. (21) obtained from electron momenta spectra recorded in C_2H_2 at $10^{14} \text{ W cm}^{-2}$ and $0.8 \mu\text{m}$ in parallel and perpendicular alignments, respectively. The quarter circle (black dashed line) represents the momentum (p_{fz}, p_{fx}) locations corresponding to $2U_p = 12 \text{ eV}$.

remains constant around 1.5 for electron final energies lower than 7 eV. Then contrary to the nearly constant ratio recorded in N_2 , the C_2H_2 ratio decreases down to 1.25 around $2U_p = 12 \text{ eV}$, reaches a maximum up to 2 around 29 eV, and finally comes back to its low-energy value at 1.5. This behavior indicates that the rescattering efficiency is much more dependent on the initial alignment in C_2H_2 than in N_2 . The energy range around $2U_p$ appears much more perturbed than in N_2 . Coming back to the angular widths in Figs. 8(a) and 8(b), we observe bumps at 8 eV and 10 eV in the angular widths from spectra recorded in parallel and perpendicular alignments, respectively, in the energy range after the above-mentioned sharp decrease from 0 eV to 6 eV. After slight decreases around $2U_p$, the angular widths increase again due to the increasing contribution of the rescattered electron signal as in the case of N_2 .

In order to get more insight in this phenomenon, we turn to the normalized difference momentum spectrum which was introduced in holography experiments by Meckel *et al.* and Walt *et al.* due to the moderate contrast between spectra recorded in parallel and perpendicular alignments [34,35]. Figure 9 presents the electron normalized difference momentum spectrum $\Delta S_{pr}(p_{fz}, p_{fx})$ spectrum defined by

$$\Delta S_{pr}(p_{fz}, p_{fx}) = \frac{S_{pr,\perp}(p_{fz}, p_{fx}) - S_{pr,\parallel}(p_{fz}, p_{fx})}{S_{pr,\perp}(p_{fz}, p_{fx}) + S_{pr,\parallel}(p_{fz}, p_{fx})}, \quad (21)$$

where the momentum spectra $S_{pr,\perp}(p_{fz}, p_{fx})$ and $S_{pr,\parallel}(p_{fz}, p_{fx})$ are recorded in perpendicular and parallel alignments, respectively. We recall that the Ozx plane is the laser wavefront plane with the axis Oz along the laser polarization direction. Most of the normalized difference spectrum is dominated by positive values as expected from more efficient tunnel ionization in perpendicular configuration. However, near the $2U_p$ circle limit and $p_{fx} = 0.15$ atomic unit appears an island with negative values where the electron signal from parallel alignment

dominates the electron signal from perpendicular alignment. On the contrary, a weak local positive maximum with a linear structure can be seen around $p_{fx} = 0.5$ atomic unit and $p_{fy} = 0.25$ atomic unit. We believe that these islands are signatures of a holographic pattern coming from interferences between the direct and rescattered electron signals. These interferences lead to a strong modulation of the ratio of angle-integrated spectra around $2U_p$ as it is observed in Fig. 8(d). No such pronounced patterns are detected in N_2 in agreement with the observed smooth ratio between spectra recorded in perpendicular and parallel alignments, respectively.

The relative behaviors of the angular widths in perpendicular and parallel alignments presented in Figs. 8(a) and 8(b) are summarized by their ratio as a function of energy in Fig. 8(c). After a first decrease with values lower than 1 at low energy due to direct ionization as it is explained in Sec. IV D, the ratio increases again for energies larger than 6 eV and reaches a maximum at around 1.25 above $2U_p = 12$ eV. Then the ratio decreases and comes back to 1 at 30 eV. This energy dependence is very similar to what is observed in N_2 . While these molecules exhibit different behaviors for direct ionization dynamics as a function of alignment, the angular dependence of rescattering above $2U_p$ is similar for both molecules: The angular distributions are larger in perpendicular alignment. Moreover this behavior is not affected by the strong modulation of the ratio of the angle-integrated spectra in C_2H_2 around $2U_p$ tentatively assigned to an interference effect between direct and rescattered electron waves.

The energy range above $2U_p$ of larger angular widths in perpendicular alignment spans up to $7U_p$ for N_2 and up to $5U_p$ for C_2H_2 . Taking a common energy range from $2U_p$ to $5U_p$ for both molecules and following Sec. II, the corresponding collision angular range is more or less in between 60° and 105° . These classical limits are established for collision-ionization phase differences larger than several times 2π rad and should be extended to include smaller phase differences. Although the classical model of Sec. II gives an over-simplified picture of rescattering, these limits allow us to discuss the influence of the molecular potential in terms of the impact parameter $b = [2E_c \tan(\Theta_c/2)]^{-1}$ in atomic units, where E_c and Θ_c are the collision energy and angle, respectively, and where the molecular potential is approximated by a bare Coulomb potential $V(r) = -1/r$. Considering the above-mentioned angular limits 60° and 105° for Θ_c , we get an impact parameter range from $0.4/E_c$ to $0.9/E_c$. For both molecules, the maximum collision energy is about $20 \text{ eV} = 0.73$ atomic unit. Although the collision energy cannot be inferred from the electron spectra, it is reasonable to estimate impact parameters in the range from less than one atomic unit to a few atomic units for which the quivering electron can utterly probe the anisotropic potential of the molecular ion after rescattering.

The decreases of the angular widths as the final energy increases do not allow us to observe a noticeable difference between parallel and perpendicular alignments for final energies larger than $5U_p$ in C_2H_2 and $7U_p$ in N_2 . We might conclude that frontal collisions, i.e., collision angles and impact parameters close to 180° and zero atomic unit, respectively, do not change the angular widths. However, much

weaker signals in this energy range and smaller angular widths may hinder the detection of any noticeable change as a function of alignment. Therefore we do not conclude yet except that an increase of electron detection efficiency is highly desirable in the high-energy range.

From the present data, it is not possible to separate the contributions of the quivering dynamics of the departing electron from that of the rescattering events leading to larger angular distributions in perpendicular alignment. Considering only the quivering dynamics, the Coulomb force exerted on the electron by symmetric linear molecular ions such as N_2^+ or $C_2H_2^+$ may be decomposed in two components. The first one is directed toward the geometric center of the structure and steers the electron toward the molecular ion independently of its orientation. The second component is parallel to the linear structure simply because the electron is more attracted by the nearest side than the farthest one. This second component might explain why the angular widths are narrower in parallel alignment for both molecules. This simple classical argument may be tested by solving numerically the time-dependent Schrödinger equation involving a single active electron and a model molecular potential. This would permit to evaluate the influence of the molecular anisotropic potential on the departing quivering electron in electron momentum spectra. These calculations require at least two spatial dimensions for molecular alignment and may be within reach with moderate computer means.

Considering only the scattering events, differential cross sections of electron collision with aligned molecular ions are not available at energies not exceeding a few tens of electronvolts. Although the use of physical quantities calculated or measured in field-free conditions remains questionable here because of the intense laser field, we believe that differential cross sections may be helpful for an improved interpretation of experimental data as well as for the development of theoretical frameworks including the multielectron dynamics in strong laser fields.

V. CONCLUSION

In summary, our objective was to probe the influence of the molecular potential on the rescattered electron leaving the molecular site in ionization of molecules induced by an intense linearly polarized laser field. For this purpose, the used laser wavelength is $0.8 \mu\text{m}$ in order to get a maximum collision energy of the order of 20 eV because higher energies would cause a too fast departure of the electron. The molecular choice N_2 and C_2H_2 relies on basically two criteria. The first one is that tunnel ionization of these linear and symmetric molecules leads to linear and symmetric ions. Therefore, rescattering is tested for two linear and symmetric structures. The second criterion relies on their opposite ionization dynamics with respect to the directions of the molecular axis and laser polarization due to their different HOMO symmetries. While N_2 is preferentially ionized when its axis is parallel to the laser polarization, the ionization of C_2H_2 favors the perpendicular configuration. In consequence, the rescattering wave packets are expected to differ strongly for both molecule when there are aligned along the same direction.

The molecules are aligned using laser-induced impulsive alignment in two directions of the laser pulse wavefront. The first one is parallel to the laser polarization direction and the second one is perpendicular to this direction. The analysis of the angle-resolved electron spectra is performed using the seminal classical model of rescattering [5,7] in order to distinguish the rescattered electron signal from the direct electron signal. The direct electron signal is analyzed using the elegant model of Murray *et al.* [37], which permits the introduction of the HOMO wave function in a simple model of electron spectrum. The observed angular widths from the angle-resolved electron spectra are thus qualitatively well understood using this model with simplified HOMO wave functions.

The classical kinematics of rescattering in strong laser fields is introduced because the final momentum of the rescattered detected electron is not the kinematic momentum just after the collision event. Although this classical model is oversimplified since it neglects the Coulomb potential, it shows that the collision momentum is encoded in a complex way in the final momentum of the detected electron. Nevertheless it allows us to get approximated ranges of the collision energy and collision angle as a function of the final energy and final angle which are the observables of experimental photoelectron angle-resolved spectra. Such a model remains a guide for the interpretation of the experimental data, but cannot constitute a valuable theoretical framework for qualitative and quantitative interpretations of the data because of the intrinsic quantum nature of the whole dynamics involving in particular multielectron effects with scattering energies not exceeding a few tens of electron volts.

In the energy range from $2U_p$ to $5U_p$, the angular widths are found to be significantly larger for N_2 and C_2H_2 molecules aligned perpendicularly to the laser polarization direction although direct ionization strongly differs regarding parallel and perpendicular alignments. In this energy range and the associated collision angle range, the lowest values of the

impact parameter are less than one atomic unit. The scattered electron approach of the ion core is sufficient for its trajectories to be influenced by the anisotropic potential because of its quivering motion while leaving the molecular site. These simple arguments may be tested numerically by solving the time-dependent Schrödinger equation with a single active electron and a model molecular potential. Although this type of calculation cannot address the multielectron dynamics of electron-ion scattering, the comparison of calculations and experimental data might be a first step to separate contributions of electron trajectories from contributions of scattering in photoelectron momentum spectra. Further theoretical efforts may focus on calculations of differential cross sections of electron-ion elastic scattering for different molecular alignments and collision energies not exceeding a few tens of electronvolts. To our knowledge these cross sections are not available yet and may be of importance for the understanding of multielectronic dynamics in strong laser fields.

More generally, these experiments point to an exciting field of theoretical research where the main question is: Can rescattering physics in strong laser field be reduced to more conventional collision physics? If laser-induced electron diffraction (LIED) [11,18–20] and the quantitative rescattering theory (QRS) [12,13,20] have solved this problem for high-energy rescattering, a lot remains to be done in the energy range of this paper, i.e., few tens of electronvolts.

ACKNOWLEDGMENTS

The technical assistance of A. Fillon and S. Foucart is gratefully acknowledged. This research is supported by a public grant from the “Laboratoire d’Excellence Physics Atoms Light Matter” (LabEx PALM) overseen by the French National Research Agency (ANR) as part of the “Investissements d’Avenir” program (reference: ANR-10-LABX-0039-PALM).

-
- [1] K. Fedus and G. P. Karwasz, *Eur. Phys. J. D* **71**, 138 (2017).
- [2] P. G. Burke, *R-Matrix Theory of Atomic Collisions* (Springer, Berlin, 2011).
- [3] M. Yu. Kuchiev, *Pis'ma Zh. Eksp. Teor. Fiz.* **45**, 319 (1987) [*Sov. Phys.-JETP Lett.* **45**, 404 (1987)].
- [4] K. J. Schafer, B. Yang, L. F. Di Mauro, and K. C. Kulander, *Phys. Rev. Lett.* **70**, 1599 (1993).
- [5] P. B. Corkum, *Phys. Rev. Lett.* **71**, 1994 (1993).
- [6] F. Krausz and M. Ivanov, *Rev. Mod. Phys.* **81**, 163 (2009).
- [7] G. G. Paulus, W. Nicklich, H. Xu, P. Lambropoulos, and H. Walther, *Phys. Rev. Lett.* **72**, 2851 (1994).
- [8] W. Becker, F. Grasbon, R. Kopold, D. Milošević, G. Paulus, and H. Walther, *Adv. At. Mol. Opt. Phys.* **48**, 35 (2002).
- [9] A. Becker and F. H. M. Faisal, *J. Phys. B: At., Mol. Opt. Phys.* **38**, R1 (2005), and references therein.
- [10] K. Amini, J. Biegert, F. Calegari, A. Chacón, M. F. Ciappina, A. Dauphin, D. K. Efimov, C. F. de Morisson Faria, K. Giergiel, P. Gniewek *et al.*, *Rep. Prog. Phys.* **82**, 116001 (2019).
- [11] T. Zuo, A. Bandrauk, and P. Corkum, *Chem. Phys. Lett.* **259**, 313 (1996).
- [12] Z. Chen, T. Morishita, A.-T. Le, and C. D. Lin, *Phys. Rev. A* **76**, 043402 (2007).
- [13] Z. Chen, A.-T. Le, T. Morishita, and C. D. Lin, *Phys. Rev. A* **79**, 033409 (2009).
- [14] M. Okunishi, T. Morishita, G. Prümper, K. Shimada, C. D. Lin, S. Watanabe, and K. Ueda, *Phys. Rev. Lett.* **100**, 143001 (2008).
- [15] D. Ray, B. Ulrich, I. Bocharova, C. Maharjan, P. Ranitovic, B. Gramkow, M. Magrakvelidze, S. De, I. V. Litvinyuk, A. T. Le *et al.*, *Phys. Rev. Lett.* **100**, 143002 (2008).
- [16] M. Meckel, D. Comtois, D. Zeidler, A. Staudte, D. Pavičić, H. C. Bandulet, H. Pépin, J.-C. Kieffer, R. Dörner, D. M. Villeneuve, and P. B. Corkum, *Science* **320**, 1478 (2008).
- [17] C. Cornaggia, *J. Phys. B: At. Mol. Opt. Phys.* **42**, 161002 (2009).
- [18] J. Xu, C. I. Blaga, K. Zhang, Y. H. Lai, C. D. Lin, T. A. Miller, P. Agostini, and L. F. DiMauro, *Nat. Commun.* **5**, 4365 (2014).
- [19] M. G. Pullen, B. Wolter, A.-T. Le, M. Baudisch, M. Hemmer, A. Senftleben, C. D. Schröter, J. Ullrich, R. Moshhammer, C. Lin, and J. Biegert, *Nat. Commun.* **6**, 7262 (2015).

- [20] C. D. Lin, A.-T. Le, C. Jin, and H. Wei, *J. Phys. B: At. Mol. Opt. Phys.* **51**, 104001 (2018).
- [21] T. Brabec, M. Y. Ivanov, and P. B. Corkum, *Phys. Rev. A* **54**, R2551 (1996).
- [22] G. L. Yudin and M. Y. Ivanov, *Phys. Rev. A* **63**, 033404 (2001).
- [23] X. L. Hao, Y. X. Bai, X. Y. Zhao, C. Li, J. Y. Zhang, J. L. Wang, W. D. Li, C. L. Wang, W. Quan, X. J. Liu *et al.*, *Phys. Rev. A* **101**, 051401(R) (2020).
- [24] X. M. Tong, Z. X. Zhao, and C. D. Lin, *Phys. Rev. A* **66**, 033402 (2002).
- [25] D. Pavičić, K. F. Lee, D. M. Rayner, P. B. Corkum, and D. M. Villeneuve, *Phys. Rev. Lett.* **98**, 243001 (2007).
- [26] S.-F. Zhao, C. Jin, A.-T. Le, T. F. Jiang, and C. D. Lin, *Phys. Rev. A* **81**, 033423 (2010).
- [27] C. Cornaggia, *J. Phys. B: At. Mol. Opt. Phys.* **49**, 19LT01 (2016).
- [28] T. Bredtmann and S. Patchkovskii, *Phys. Rev. A* **99**, 063424 (2019).
- [29] L. V. Keldysh, *J. Exptl. Theoret. Phys.* **47**, 1945 (1964) [*Sov. Phys. JETP* **20**, 1307 (1965)].
- [30] Y. Huismans, A. Rouzée, A. Gijsbertsen, J. H. Jungmann, A. S. Smolkowska, P. S. W. M. Logman, F. Lépine, C. Cauchy, S. Zamith, T. Marchenko *et al.*, *Science* **331**, 61 (2011).
- [31] T. Marchenko, Y. Huismans, K. J. Schafer, and M. J. J. Vrakking, *Phys. Rev. A* **84**, 053427 (2011).
- [32] X.-B. Bian, Y. Huismans, O. Smirnova, K.-J. Yuan, M. J. J. Vrakking, and A. D. Bandrauk, *Phys. Rev. A* **84**, 043420 (2011).
- [33] Y. Huismans, A. Gijsbertsen, A. S. Smolkowska, J. H. Jungmann, A. Rouzée, P. S. W. M. Logman, F. Lépine, C. Cauchy, S. Zamith, T. Marchenko *et al.*, *Phys. Rev. Lett.* **109**, 013002 (2012).
- [34] M. Meckel, A. Staudte, S. Patchkovskii, D. M. Villeneuve, P. B. Corkum, R. Dörner, and M. Spanner, *Nat. Phys.* **10**, 594 (2014).
- [35] S. G. Walt, N. Bhargava Ram, M. Atala, N. Shvetsov-Shilovski, A. von Conta, D. Baykusheva, M. Lein, and H. J. Wörner, *Nat. Commun.* **8**, 15651 (2017).
- [36] A. M. Perelomov, V. S. Popov, and M. V. Terent'ev, *J. Exptl. Theoret. Phys.* **51**, 309 (1966) [*Sov. Phys. JETP* **24**, 207 (1967)].
- [37] R. Murray, W.-K. Liu, and M. Y. Ivanov, *Phys. Rev. A* **81**, 023413 (2010).
- [38] T. Seideman, *Phys. Rev. Lett.* **83**, 4971 (1999).
- [39] F. Rosca-Pruna and M. J. J. Vrakking, *Phys. Rev. Lett.* **87**, 153902 (2001).
- [40] C. Cornaggia, *Phys. Rev. A* **91**, 043426 (2015).
- [41] C. Cornaggia, *J. Phys. B: At. Mol. Opt. Phys.* **46**, 191001 (2013).
- [42] G. Herzberg, *Molecular Spectra and Molecular Structure*, Vol. III, Electronic Spectra and Electronic Structure of Polyatomic Molecules (D. Van Nostrand Company, New York, 1966).
- [43] P. Linstrom and W. Mallard (eds.), *NIST Chemistry Web-Book*, Vol. NIST Standard Reference Database Number 69 (National Institute of Standards and Technology, Gaithersburg, MD, 2018), <https://doi.org/10.18434/T4D303>.
- [44] R. R. Freeman, P. H. Bucksbaum, H. Milchberg, S. Darack, D. Schumacher, and M. E. Geusic, *Phys. Rev. Lett.* **59**, 1092 (1987).
- [45] S. Petretti, Y. V. Vanne, A. Saenz, A. Castro, and P. Decleva, *Phys. Rev. Lett.* **104**, 223001 (2010).
- [46] R. Murray, M. Spanner, S. Patchkovskii, and M. Y. Ivanov, *Phys. Rev. Lett.* **106**, 173001 (2011).